Supplementary Information

Inhibiting recombination to improve the performance of plasma-based CO_2 conversion

Kaiyi Wang[a,1], Sara Ceulemans[b,1], Hao Zhang[a,c]*, Ivan Tsonev[b], Yilin Zhang[a], Yanhui Long[a], Mengxiang Fang[c], Xiaodong Li[a], Jianhua Yan[a], Annemie Bogaerts[b,*]

a. State Key Laboratory of Clean Energy Utilization, Zhejiang University, Hangzhou 310027, China

b. Research group PLASMANT, Department of Chemistry, University of Antwerp, Wilrijk-Antwerp BE-2610, Belgium

c. Zhejiang University Qingshanhu Energy Research Center, 311305 Hangzhou, P. R. China

[1.] These authors contributed equally to this work.

* Corresponding authors:

zhang_hao@zju.edu.cn (H. Zhang);

annemie.bogaerts@uantwerpen.be (A. Bogaerts)

Table of contents

S1 Experimental setup

A schematic of the experimental setup is presented in Fig. S1, consisting of gas feeding system, power supply, plasmatron reactor with gas sampling set, oscilloscope with high-voltage probe and current probe for electrical parameter measurement, and gas analyser for gas composition analysis.

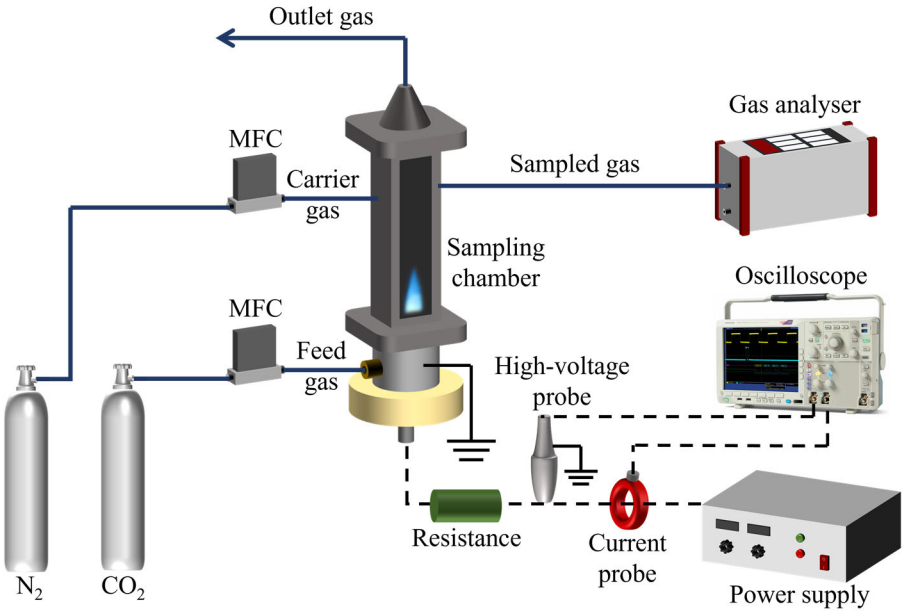

Fig. S1. Schematic of the experimental setup

The gas temperature in the sampling tube was estimated in the range of 400-600 K, based on the calculation given below:

We assumed that it was an isobaric adiabatic mixing process.

Gas flow rate: $m_c = 1.25\ g/min$, $m_s = 0.6\ g/min$

Gas temperature before mixing: $T_{1c} = 300\ K$, $T_{1s} = 500{\sim}1300\ K$

where m_c and m_s are the mass flow rates of carrier gas and sampled gas, respectively; T_{1c} and T_{1s} are the initial temperature of carrier gas and sampled gas, respectively.

Gas temperature after mixing:

$$T_2 = \frac{m_c \bar{c}_{p,c} T_{1c} + m_s \bar{c}_{p,s} T_{1s}}{m_c \bar{c}_{p,c} + m_s \bar{c}_{p,s}} \qquad (S1)$$

where $\bar{c}_{p,c}$ and $\bar{c}_{p,s}$ are the average specific heat at constant pressure. Since they are very similar, we assume that they are equal here. Thus, $T_2 \approx 400{\sim}600\ K$.

S2 Model description

The model is calculated using COMSOL Multiphysics and is a fully coupled combination of calculating the gas velocity and pressure, temperature, species concentrations and how these species are distributed over the reactor.

S2.1 Gas flow

The laminar gas flow is calculated using the Navier-Stokes equations for conservation of mass and momentum in their time-dependent form:

$$\frac{\partial \rho}{\partial t} + \nabla \cdot (\rho \vec{u}) = 0 \qquad (S2)$$

$$\rho \frac{\partial \vec{u}}{\partial t} + \rho(\vec{u} \cdot \nabla)\vec{u} = \nabla \cdot \left[-p\vec{I} + \mu(\nabla \vec{u} + (\nabla \vec{u})^T) - \frac{2}{3}\mu(\nabla \cdot \vec{u})\vec{I} \right] \qquad (S3)$$

With ρ the gas density, t the time, $\vec{u}$ the gas velocity vector, p the pressure, $\vec{I}$ the identity matrix, μ the dynamic viscosity, and superscript T stands for the transpose of the velocity vector gradient. These equations are solved to obtain the velocity and pressure as a function of time and position in the 3D and 2D axisymmetric geometry. The flow is considered weakly compressible, which means that the density only depends on temperature, but does not vary with pressure. For the 3D model, the gas flow is assumed to be compressible, in which the density depends on both temperature and pressure.

The boundary conditions are divided into the inlet, the outlet and the walls.

(a) Inlet

The boundary condition at the inlet is given by:

$$\vec{u} = \overrightarrow{u_0} \qquad (S4)$$

The velocity $\overrightarrow{u_0}$ set at the inlet is obtained from the 3D gas flow model. A cross-section plane is defined in the 3D model at the height at which the 2D axisymmetric model starts, i.e., at -15 mm. On this plane, different concentric circles are drawn, with varying radii that correspond to specific values of r, and therefore specific points along the inlet line, corresponding to a surface, in the 2D axisymmetric model. A schematic drawing of the cross-section surface, the concentric circles and the velocity components is given in Fig. S2. For every radius, i.e., for every point along the inlet line, the velocity is calculated as the average velocity over the complete circle. This velocity consists of three velocity components, an r-, phi- and z-component in cylindrical coordinates that are each calculated separately and imposed separately on the inlet boundary in the 2D axisymmetric model. Because the phi-component of the velocity is not equal to 0 m/s on this plane, the swirl in the flow is included in the 2D axisymmetric model. The three velocity components in cylindrical coordinates are obtained from the velocities in Cartesian coordinates in the 3D model using the following equations:

$$v_r = \frac{xv_x + yv_y}{\sqrt{x^2 + y^2}} \tag{S5}$$

$$v_\varphi = -\sqrt{{v_x}^2 + {v_y}^2} \times \sin\left(\cos^{-1}\left(\frac{xv_x + yv_y}{\sqrt{x^2 + y^2}\sqrt{{v_x}^2 + {v_y}^2}}\right)\right) \tag{S6}$$

$$v_z = v_z \tag{S7}$$

With x, y and z the Cartesian coordinates in the 3D model of the points on the circle, and v_x, v_y and v_z the three velocity components in Cartesian coordinates in the same point.

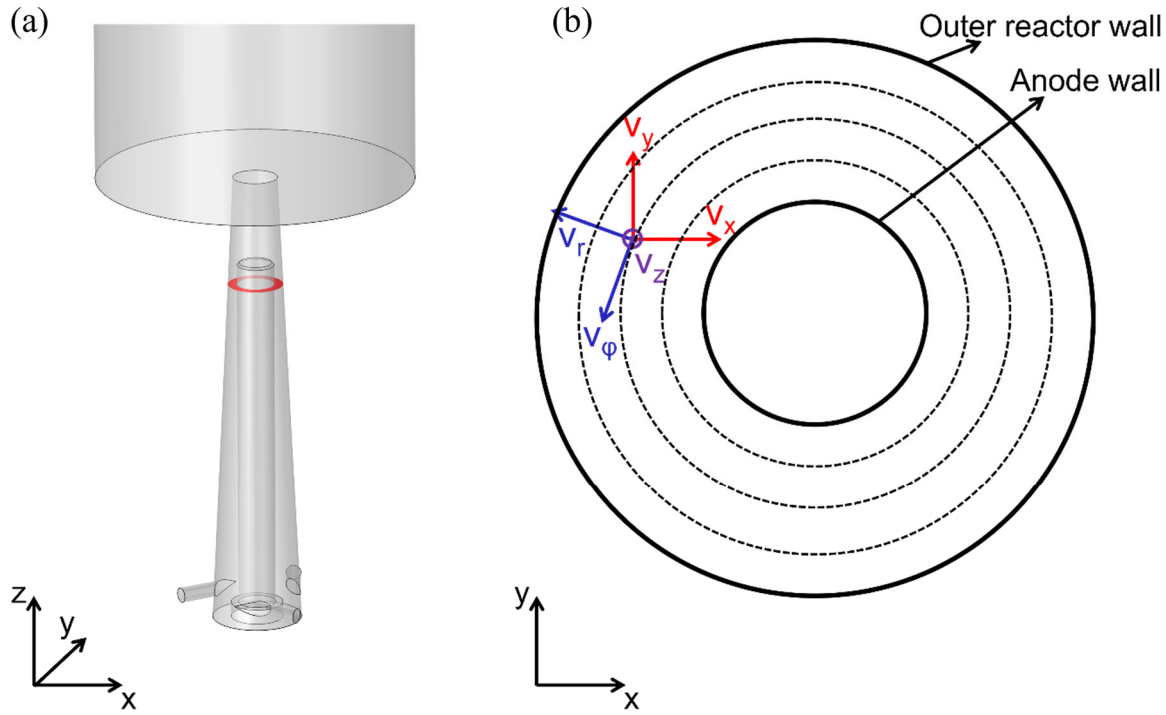

Fig. S2. (a) Drawing of the reactor part and start of the exhaust in the 3D model, indicating the ring-shaped cross-section surface at z = -15 mm (in red) that is used to obtain the velocity components for the 2D axisymmetric model, and (b) schematic drawing of the cross-section surface with the velocity components in Cartesian (in red) and cylindrical (in blue) coordinates indicated. The z-component of the velocity is pointing out of the page. The dashed concentric circles correspond to the different *r*-values at which the velocity components are calculated (more than the three circles shown here), as an average over one of these circles.

(b) Outlet

The outlet is defined as an open boundary and given by:

$$\left[-p\vec{I} + \mu(\nabla\vec{u} + (\nabla\vec{u})^T) - \frac{2}{3}\mu(\nabla \cdot \vec{u})\vec{I}\right]\vec{n} = \vec{0} \tag{S8}$$

With $\vec{n}$ a unity vector normal to the outlet boundary and pointing out of the reactor.

(c) Walls

All walls have a no slip condition:

$$\vec{u} = \vec{0} \tag{S9}$$

S2.2 Heat transfer

The heat transfer module calculates the temperature through the heat balance equation:

$$\rho C_p \frac{\partial T}{\partial t} + \rho C_p \vec{u} \cdot \nabla T + \nabla \cdot \vec{q} = Q_p + Q_{vd} + Q_{heat\ source} + Q_{heat\ sink} \tag{S10}$$

$$\vec{q} = -k \nabla T \tag{S11}$$

$$Q_p = \alpha_p T \left(\frac{\partial p}{\partial t} + \vec{u} \cdot \nabla p \right) \tag{S12}$$

$$Q_{vd} = \tau : \nabla \vec{u} \tag{S13}$$

With C_p the specific heat capacity at constant pressure, T the temperature, $\vec{q}$ the conductive heat flux, Q_p the heat corresponding to work resulting from pressure changes, Q_{vd} the heat due to viscous dissipation, while $Q_{heat\ source}$ and $Q_{heat\ sink}$ are the heat source and heat sink defined in our model, representing the plasma and accounting for cooling in the afterglow, respectively. Note that the heat sink has a negative value. The terms on the left-hand side in equation (S10) are the change in temperature over time, the convective and conductive heat transfer, respectively. Furthermore, in equations (S11-S13), k is the thermal conductivity, α_p the coefficient of thermal expansion, and τ the viscous stress tensor. The shape of the heat source and heat sink is indicated in Fig. 2 in the main paper, and the total power is then distributed over these shapes using two rectangle functions, in the r-direction and z-direction, with rounded edges; through the 2D axisymmetry of the model, together they create a cylindrical shape. Because the functions are rectangles, the powers are approximately equally distributed over the cylinders, except at the edges where there is a lower power distribution due to the rounding of these edges. Together, these equations provide the temperature as a function of time and position in the 2D axisymmetric geometry.

In the model, we use a heat sink to represent the effect of turbulent cooling. Indeed, we assume that the flow is laminar, to reduce complexity and computation time, but this means that turbulent heat transfer is not included. However, modelling of a gliding arc plasmatron reactor has revealed that turbulent heat transfer can become important, with a turbulent gas thermal conductivity about 100 times larger than the gas thermal conductivity without turbulence for an argon plasma [1]. In addition, it has also been demonstrated experimentally that the turbulence causes radial mixing after the plasma, by using Schlieren photographs [2]. The latter paper clearly shows the effect of plasma on the flow behaviour:

without plasma, the flow is laminar, but when a voltage is applied, the flow behaves turbulently and more mixing takes place, which can also happen in our setup but is not yet accounted for in the model.

This turbulence is caused by the movement of the arc. Based on the current-voltage curves and a video of the plasma measured during the experiment, we know that the arc is in so-called restrike mode. In this mode, reattachment of the arc takes place, which influences the flow significantly [3]. In this way, the distribution of heat, and therefore temperature, and particles will also be changed to some extent. However, modelling this restrike phenomenon requires more complicated models, including a more elaborate description of the (boundary layer of the) anode and a 3D geometry [3]. This would lead to excessive computation times, in combination with the calculation of the chemistry and particle transport, keeping in mind also the size of this reactor. Therefore, we use the above-described heat sink, to mimic the effect of turbulence and reattachment on the gas temperature. Because this turbulence, and therefore cooling, increases with increasing flow rates, we used a somewhat higher power of the heat sink at 7 L/min (i.e., 185 W) compared to 160 W at 5 L/min.

There are more separate boundary conditions for the heat transfer compared to the gas flow.

(a) Inlet

The inlet boundary condition is given by:

$$T = T_0 = 300\ K \tag{S14}$$

The temperature at the inlet is set to a constant value of the 300K. This corresponds to CO_2 gas that flows into the reactor at room temperature.

(b) Outlet

The heat transfer at the outlet has the following boundary condition:

$$-\vec{n} \cdot \vec{q} = 0 \tag{S15}$$

This means that there is no conductive heat flux through the outlet, both into and out of the reactor. As a consequence, heat inside the exhaust can only be transported out of the reactor outlet through convection, transported by the gas flow.

(c) Walls at the outside of the reactor and the start of the exhaust (orange in Fig. 2 of the main paper)

These walls are in contact with the air outside the reactor, and in close contact with the heat source, and are defined by a heat flux through the wall:

$$-\vec{n} \cdot \vec{q} = h(T_{ext} - T) \tag{S16}$$

The heat transfer by conduction for these walls is set to a certain value, calculated using the heat transfer coefficient h (in this case equal to 50 W/(m^{2}K)), the external temperature of the air outside the reactor T_{ext} (here a constant value of 293.15 K), and the temperature at the wall inside the reactor T. When the

temperature T is higher than the external temperature, which is mostly the case, the heat conduction is directed outwards and the heat from the reactor is lost to the outside environment.

(d) Cylinder side (brown in Fig. 2 of the main paper)

The cylinder side has the same boundary condition as the inlet, namely:

$$T = T_0 = 300\ K \tag{S17}$$

Because there is no gas flow into or out of this wall, this boundary condition here means that the gas temperature close to the wall is set to 300 K.

(e) Anode walls and walls at the end of the exhaust (pink and purple, respectively, in Fig. 2 of the main paper):

These two separate groups of boundaries have the same thermal insulation boundary condition:

$$-\vec{n} \cdot \vec{q} = 0 \tag{S18}$$

This equation indicates that there is no conduction through these walls. The anode walls are, similar to the walls at the outside of the reactor, close to the heat source and in contact with high temperature gas. However, these walls are not directly connected to the room temperature gas surrounding the reactor. Therefore, they are given a thermal insulation boundary condition instead of a heat flux boundary condition.

S2.3 Chemistry and transport of chemical species

Modelling chemical transport includes both the reactions taking place inside the reactor, as well as the transport of the different species through the reactor. The transport equation for the different species, taking into account the conservation of mass, is based on the following equation:

$$\rho \frac{\partial \omega_i}{\partial t} + \nabla \cdot \vec{j_i} + \rho(\vec{u} \cdot \nabla)\omega_i = R_i \tag{S19}$$

With ω_i the mass fraction of species i, $\vec{j_i}$ the mass flux of species i relative to the mass-averaged velocity and R_i the total net rate of production and destruction of species i. The terms on the left-hand side represent the change in mass fraction of species i over time, the diffusion of species i and its transport due to the gas flow, respectively, while the right-hand side corresponds to the change in species i due to reactions taking place in the reactor. This equation is used for four species included in the model, CO, O, O_2 and C, and these four equations are solved together to calculate their mass fractions, as a function of time and position in the 2D axisymmetric geometry. The mass fraction of CO_2 is obtained from the assumption that the sum of all mass fractions is equal to 1.

The mass flux $\vec{j_i}$ used in the mass transport equation corresponds to molecular diffusion and is calculated as:

$$\vec{J_i} = -\left(\rho D_i^m \nabla \omega_i + \rho \omega_i D_i^m \frac{\nabla M_n}{M_n} - \rho \omega_i \sum_{i=1}^{N} \frac{M_i}{M_n} D_i^m \nabla x_i\right) \quad (S20)$$

$$D_i^m = \frac{1 - \omega_i}{\sum_{k \neq i}^{N} \frac{x_k}{D_{ik}}} \quad (S21)$$

$$M_n = \left(\sum_{i=1}^{N} \frac{\omega_i}{M_i}\right)^{-1} \quad (S22)$$

$$D_{ik} = 2.662821 \cdot 10^{-22} \frac{\sqrt{T^3 \frac{(M_i + M_k)}{(2 \cdot 10^3 M_i M_k)}}}{p \sigma_i \sigma_k \Omega_{D,diff}} \quad (S23)$$

$$\Omega_{D,diff} = \frac{c_1}{(T^*)^{c_2}} + \frac{c_3}{e^{c_4 T^*}} + \frac{c_5}{e^{c_6 T^*}} + \frac{c_7}{e^{c_8 T^*}} \quad (S24)$$

$$T^* = T \frac{k_B}{\sqrt{\varepsilon_i \varepsilon_k}} \quad (S25)$$

With D_i^m the mixture-averaged diffusion coefficient of species i, M_n the mean molar mass, M_i and M_k the molar mass of species i and k, respectively, x_i the mole fraction of species i, D_{ik} the multicomponent Maxwell-Stefan diffusivities for species i and k, σ_i and σ_k the potential characteristic length value of species i and k, and $\Omega_{D,diff}$ a collision integral used to calculate diffusion coefficients. c_1 to c_8 are eight empirical constants, k_B is the Boltzmann constant and ε_i and ε_k the potential energy minimum of species i and k. The potential characteristic lengths and potential energy minima are obtained from GRI-Mech 3.0 [4]. The sum is taken over all N species in equations (S20) and (S22), and over all species k, except i itself, in equation (S21). In this model, a mixture-averaged diffusion model is applied, which uses a Fick's law type approximation. In this approximation, the net diffusive mass flux is not equal to 0, which is why a correction term is added. This is the last term on the right-hand side of equation (S20).

The total net rate of production and destruction of species i, R_i in equation (S19), is calculated with the formula:

$$R_i = \sum_{j=1}^{M} \nu_{ij} r_j \quad (S26)$$

where r_j is the net rate of reaction j, calculated as:

$$r_j = k_j^f \prod_{i \in react} c_i^{-\nu_{ij}} - k_j^r \prod_{i \in prod} c_i^{\nu_{ij}} \quad (S27)$$

In these equations, ν_{ij} is the stoichiometric coefficient of species i in reaction j, the sum is taken over all M reactions, k_j^f and k_j^r are the forward and reverse rate coefficients of reaction j, respectively, c_i is

the molar concentration of species i, and the equation is split in terms calculating the forward reaction rate when i is a reactant and a reverse rate when i is a product.

The equations of the forward rate coefficients are given in Table 1 in the main paper. The reverse rate coefficients are calculated through detailed balancing, using the following equations [5]:

$$k_j^r = \frac{k_j^f}{K_j} \tag{S28}$$

$$K_j = e^{\left(\frac{\Delta S_j^0}{R} - \frac{\Delta H_j^0}{RT}\right)} \left(\frac{P_{atm}}{RT}\right)^{\sum_{i=1}^{N} \nu_{ij}} \tag{S29}$$

$$\Delta S_j^0 = \sum_{i=1}^{N} \nu_{ij} S_i^0 \tag{S30}$$

$$\Delta H_j^0 = \sum_{i=1}^{N} \nu_{ij} H_i^0 \tag{S31}$$

With K_j the equilibrium constant of reaction j, ΔS_j^0 and ΔH_j^0 the standard-state molar entropy and enthalpy of reaction j, respectively, R the gas constant, P_{atm} atmospheric pressure (101325 Pa), and S_i^0 and H_i^0 the standard-state molar entropy and enthalpy of species i, which are calculated using NASA polynomials [6]. The sum in these equations is calculated over all N species i in reaction j.

The changing composition of the gas influences the properties of this gas. The density is calculated using the ideal gas law, while the other gas properties are calculated using the following formulas.

(i) Heat capacity C_p:

$$C_p = \sum_{i=1}^{N} \omega_i \frac{C_{p,i}}{M_i} \tag{S32}$$

With $C_{p,i}$ the heat capacity at constant pressure for species i, which is obtained using NASA polynomials [6], and the other parameters are defined in earlier equations.

(ii) Dynamic viscosity μ:

$$\mu = \sum_{i=1}^{N} \frac{\mu_i}{1 + \frac{1}{x_i} \sum_{k \neq i}^{N} x_k \phi_{ik}} \tag{S33}$$

$$\phi_{ik} = \frac{\left[1 + \left(\frac{\mu_i}{\mu_k}\right)^{0.5} \left(\frac{M_k}{M_i}\right)^{0.25}\right]^2}{2\sqrt{2}\left[1 + \frac{M_i}{M_k}\right]^{0.5}} \tag{S34}$$

$$\mu_i = 2.669 \cdot 10^{-6} \frac{\sqrt{T M_i \cdot 10^3}}{{\sigma_i}^2 \Omega_{D,visc}} \tag{S35}$$

$$\Omega_{D,visc} = \frac{b_1}{(T^*)^{b_2}} + \frac{b_3}{e^{b_4 T^*}} + \frac{b_5}{e^{b_6 T^*}} + \frac{4.998 \cdot 10^{-40} {\mu_{D,i}}^4}{{k_B}^2 T \left(\frac{\varepsilon_i}{k_B}\right) {\sigma_i}^6} \quad (S36)$$

$$T^* = T \frac{k_B}{\varepsilon_i} \quad (S37)$$

Where μ_i and μ_k are the dynamic viscosity of species i and k, and $\Omega_{D,visc}$ another, dimensionless collision integral used to calculate the viscosity and thermal conductivity, b_1 to b_6 are empirical constants and $\mu_{D,i}$ is the dipole moment of species i, also obtained from GRI-Mech 3.0 [4]. More information on the two collision integrals $\Omega_{D,diff}$ (equation (S24)) and $\Omega_{D,visc}$ (equation (S36)) can be found in references 4 and 5. The sum in equation (S33) is taken over all N species at the start of the right-hand side and all N species, except species i itself, in the denominator.

(iii) Thermal conductivity k:

$$k = \frac{1}{2}\left(\sum_{i=1}^{N} x_i k_i + \frac{1}{\sum_{i=1}^{N} \frac{x_i}{k_i}}\right) \quad (S38)$$

$$k_i = \mu_i \cdot \frac{1.15 C_{p,i} + 0.88R}{M_i} \quad (S39)$$

With x_i the mole fraction of species i, k_i the thermal conductivity of this species, μ_i the viscosity of species i, defined above in equation (S35) and $C_{p,i}$ the heat capacity at constant pressure of i.

The boundary conditions for the chemical transport are as follows:

(a) Inlet

The boundary condition at the inlet is given by:

$$\omega_i = \frac{x_{0,i} M_i}{M_n} \quad (S40)$$

with $x_{0,i}$ the mole fraction of every species i at the inlet, and the other parameters defined above. The inlet has a set mole fraction, converted to mass fraction, for all five species. For CO, O_2, O and C, these initial mole fractions are equal to 10^{-8}, which means that the mole fraction of CO_2 is equal to $1 - 4 \times 10^{-8}$. This value of 10^{-8} is chosen instead of 0 for numerical reasons, to let the simulation calculate more smoothly.

(b) Outlet

The mass transport at the outlet is defined as:

$$-\vec{n} \cdot \rho D_i^m \nabla \omega_i = 0 \quad (S41)$$

This means that there is no mass diffusion of any species i possible through the outlet, and species can only be removed from the reactor by the gas flow. This is similar to the outlet boundary condition for heat transfer, where only convection by the gas flow can transport heat from the reactor, but not conduction.

(c) Walls

All walls have a no flux boundary condition:

$$-\vec{n} \cdot \vec{j_i} = 0 \qquad (S42)$$

This simply means that there is no mass transfer through the walls.

S3 Detailed calculation results

S3.1 Gas flow pattern in the reactor and exhaust

As can be seen from Fig. S3, the gas flows upwards in the centre of the reactor, coming directly from the inlet, and also flows upwards close to the walls. In between those two upward gas streams, there is a downwards flow. The latter is caused by the converging end of the reactor, close to the outlet. Part of the gas collides with this converging wall and recirculates back in the exhaust, taking the heat and higher concentration in CO and O_2 with it, and spreading it over the exhaust, away from the symmetry axis.

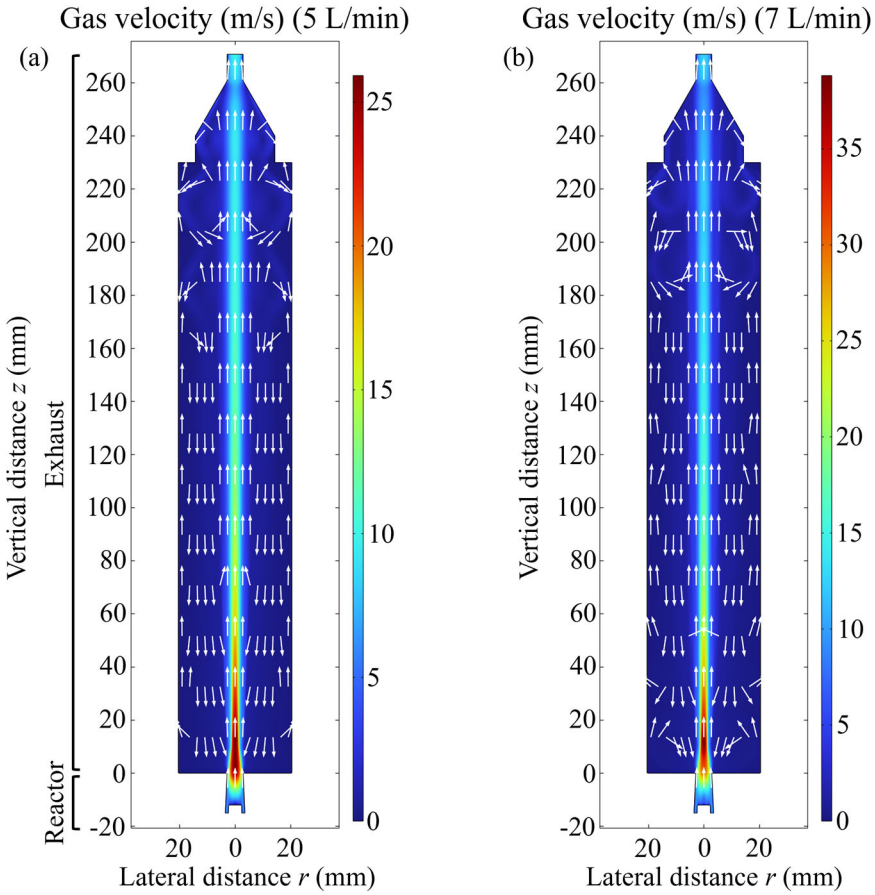

Fig. S3. Total flow velocity in the reactor and exhaust for (a) 5 L/min and (b) 7 L/min. The arrows indicate the direction of the flow in the points at the tails of the arrows.

S3.2 Reaction analysis

Figs. S4 and S5 present the reaction rates of the two CO_2 conversion reactions, and their splitting and recombination components for 7 L/min, similar to Figs. 5 and 6 for 5 L/min in the main paper. The plots look very similar to the results at 5 L/min, but with two larger differences. Firstly, the reaction rates, especially the recombination rate of reaction 1, are slightly more spread out to higher z-values in the afterglow for the higher flow rate of 7 L/min, which is a logical consequence of the increased convective heat transport in the axial direction, transporting the heat to higher positions in the reactor, although this difference is not always very clear. Secondly, the high temperature, and therefore the reaction rates, seem to be less attached to the anode at 7 L/min, which is also caused by the gas flow itself.

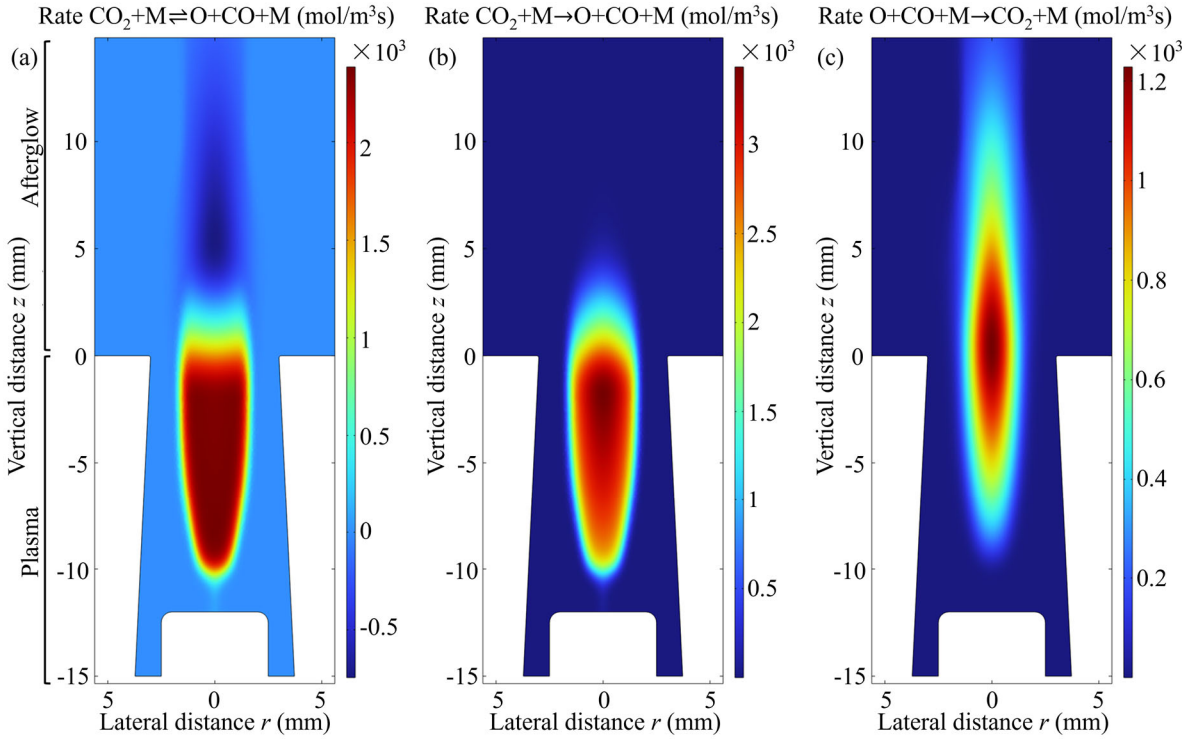

Fig. S4. Net rate of CO_2 conversion by the reaction $CO_2 + M \rightleftharpoons O + CO + M$ (a), and its breakdown into the splitting rate (forward reaction) (b) and the recombination rate (backward reaction) (c), at 7 L/min. The plasma is located at $z < 0$ mm, and the afterglow starts when the gas leaves the reactor and enters the exhaust at $z > 0$ mm.

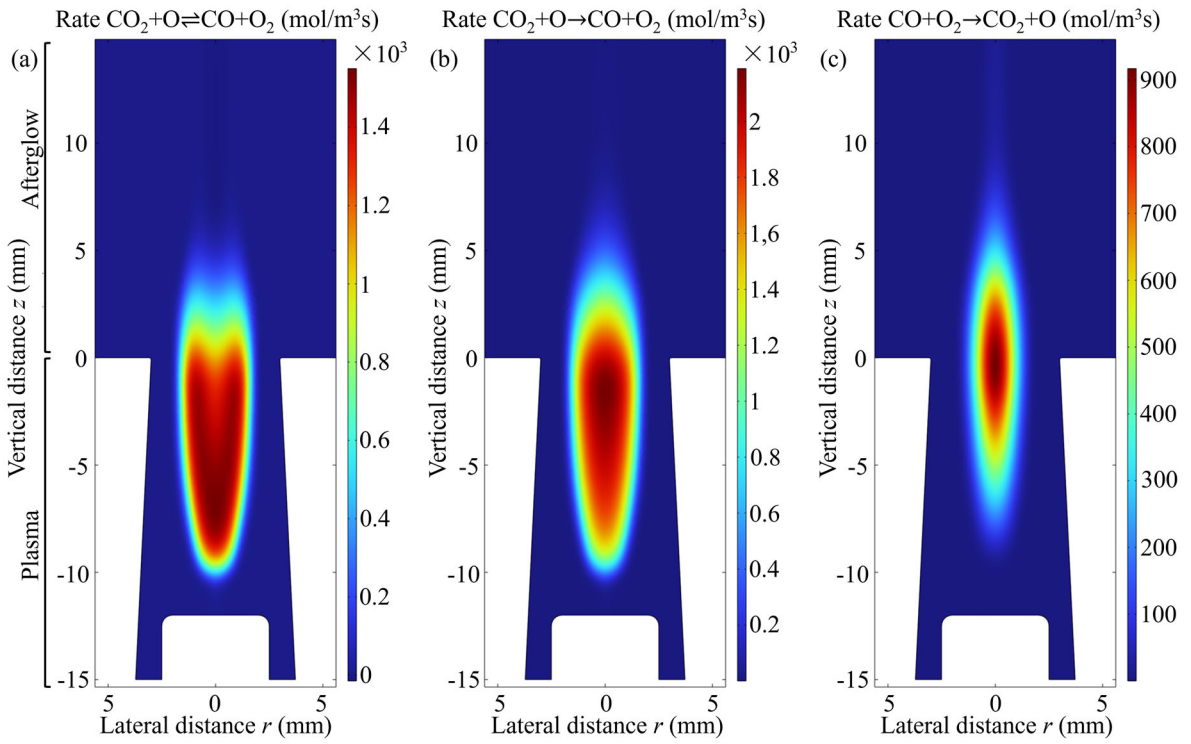

Fig. S5. Net rate of CO_2 conversion by the reaction $CO_2 + O \rightleftharpoons CO + O_2$ (a), and its breakdown into the splitting rate (forward reaction) (b) and the recombination rate (backward reaction) (c), at 7 L/min. The plasma is located at $z < 0$ mm, and the afterglow starts when the gas leaves the reactor and enters the exhaust at $z > 0$ mm.

Fig. S6 illustrates the concentration of O atoms in the reactor and the start of the exhaust. The O atom concentration remains relatively high in the first few millimetres of the exhaust and only drops below 1 % of its maximum value along the central axis at 22.2 mm and 33.1 mm (not visible in the plots), for 5 and 7 L/min, respectively.

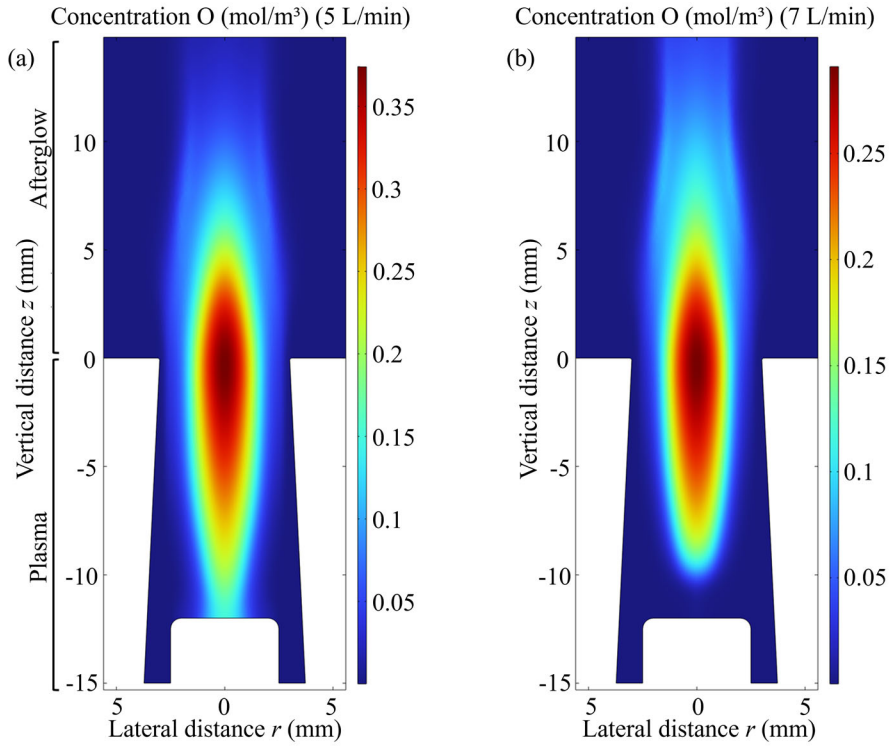

Fig. S6. Concentration of O atoms in the reactor and the start of the exhaust for 5 L/min (a) and 7 L/min (b).

S4 Afterglow quenching

The relative improvements of CO_2 conversion in Fig. 10 were calculated as below:

$$Relative\ improvement\ (as\ factor) = \frac{X_{CO_2}^{UC}(\%) - X_{CO_2}^{\overline{OC}^{W}}(\%)}{X_{CO_2}^{\overline{OC}^{W}}(\%)} \quad (S43)$$

where $X_{CO_2}^{UC}$ is the CO_2 conversion with solely upstream cooling, but the same formula applies for the CO_2 conversion with solely downstream cooling ($X_{CO_2}^{DC}$) or with both cooling ($X_{CO_2}^{UC+DC}$); $X_{CO_2}^{W/OC}$ is the CO_2 conversion without cooling. The relative improvements of energy efficiency were calculated in the same way; just replacing X with η.

The proportion of input energy used for gas heating was estimated by calculating the energy required to heat the inlet gas (pure CO_2) to 1200°C, assuming this heating process is carried out at constant pressure. It should be noted that the calculated values here are only estimates.

Discharge power: 480W

Inlet flow rate Q_{in}: $Q_{in} = 6\ L/min\ (273\ K, 101325\ Pa)$

Inlet temperature T_1: $T_1 = 20$℃, outlet temperature T_2: $T_2 = 1200$℃

Inlet mass flow rate M_{in}:

$$M_{in}(g/s) = \frac{Q_{in}(L/\mathrm{min}) \times 1.977(g/L)}{60(s/\mathrm{min})} = 0.1977(g/s) \quad (S44)$$

Gas heat absorption power q:

$$q(W) = M_{in}(g/s) \times (\bar{c}_{p_0}^{T_2}(J/(g \cdot K)) \times T_2(℃) - \bar{c}_{p_0}^{T_1}(J/(g \cdot K)) \times T_1(℃)) = 270\ W \quad (S45)$$

where $\bar{c}_{p_0}^{T}$ is the average specific heat at constant pressure for the gas as it is heated from 0°C to temperature t (°C). $\bar{c}_{p_0}^{20} = 0.825 J/(g \cdot K)$, $\bar{c}_{p_0}^{1200} = 1.153 J/(g \cdot K)$

Thus, about 56% of input energy is used for gas heating.

References

[1] G. Trenchev, S. Kolev, W. Wang, M. Ramakers, A. Bogaerts, CO2 Conversion in a Gliding Arc Plasmatron: Multidimensional Modeling for Improved Efficiency, J. Phys. Chem. C. 121 (2017) 24470-24479. http://doi.org/10.1021/acs.jpcc.7b08511.

[2] F. Liu, B. Zhang, Z. Fang, M. Wan, H. Wan, K.K. Ostrikov, Jet-to-jet interactions in atmospheric-pressure plasma jet arrays for surface processing, Plasma Process. Polym. 15 (2018). http://doi.org/10.1002/ppap.201700114.

[3] J.P. Trelles, C. Chazelas, A. Vardelle, J.V.R. Heberlein, Arc Plasma Torch Modeling, J. Therm. Spray Technol. 18 (2009) 728-752. http://doi.org/10.1007/s11666-009-9342-1.

[4] G.P. Smith, D.M. Golden, M. Fenklach, N.W. Moriarty, B. Eiteneer, M. Goldenberg, C.T. Bowman, R.K. Hanson, S. Song, W.C. Gardiner Jr., V.V. Lissianski, Z. Qin, GRI-Mech 3.0, http://combustion.berkeley.edu/gri-mech/version30/text30.html.

[5] Reaction Design. ANSYS Chemkin Theory Manual 17.0 (15151), San Diego, 2015.

[6] B. McBride, M. Zehe, S. Gordon, NASA Glenn Coefficients for Calculating Thermodynamic Properties of Individual Species, 2002.